Robust Perspective-n-Crater for Crater-based Camera Pose Estimation

Supplementary Material

8. Conic to ellipse equation

An ellipse $\mathbf{e} = (x, y, a, b, \theta)$, can be formed from conic $\mathbf{D}$ (1), where $\mathbf{x} = [x, y]$ is the ellipse centre, $\mathbf{r} = [a, b]$ is the ellipse semi-major and semi-minor axes, and θ is the angle of orientation,

$$x = \frac{2OQ - IS}{I^2 - 4JO} \tag{35}$$

$$y = \frac{2JS - IQ}{I^2 - 4JO} \tag{36}$$

$$a, b = \sqrt{\frac{2(JS^2 + OQ^2 - IQS + U(I^2 - 4JO))}{(I^2 - 4JO)(\pm\sqrt{(J-O)^2 + I^2} - J - O))}} \tag{37}$$

$$\theta = \begin{cases} \frac{\pi}{2} & \text{if } I = 0 \text{ and } J > O \\ \frac{\cos^{-1}\frac{J-O}{I}}{2} & \text{if } I \neq 0 \text{ and } J \leq O \\ \frac{\pi}{2} + \frac{\cos^{-1}\frac{J-O}{I}}{2} & \text{if } I \neq 0 \text{ and } J > O \\ 0 & \text{otherwise} \end{cases} \tag{38}$$

9. Dataset generation

9.1. Image generation

Four DEMs from the PDS data node [25] of 45 degrees latitude and longitude were selected to make up the dataset. These patches were chosen based on scientific interest (regions in the North and South Poles), and regions of highest and lowest crater densities. For each DEM, the camera was situated at an altitude of 100km from every visible crater in the crater catalogue. At each of these positions, seven images were taken at increments of 10 degrees off nadir, starting at nadir pointing. PANGU returned the image alongside the ground truth pose of the camera, which was later used to project craters onto the image plane. Note that as the DEMs were loaded in sections, the imaged surface appeared cut off if taken too close to the DEM boundary. If less than 60% of the image consisted of the DEM surface, we discarded the image to ensure fair distribution of crater detections.

9.2. Simulating crater detections

A simulated CDA was implemented to emulate realistic crater detections. The initial set of conditions to see if a projected crater from the crater catalogue would be detectable by a CDA were that:

- The majority of the crater rim must lie in the image plane. CDAs tend not to detect craters that are cut off in the image, as their ellipse estimate is unreliable.
- The angle between the crater's plane normal and the camera line of sight has to be less than or equal to 75 degrees. When this angle exceeds 75 degrees, the craters tend to be too far away from the camera to be detectable.
- The projected crater's semi-minor axis has to be greater than ten pixels, or alternatively, the semi-minor axis has to be greater than five pixels and more than 75% of the semi-major axis, otherwise the crater would be too small to be detected.
- The craters in the crater catalogue had basins that were considered deep if the ratio of the difference in median rim height and median crater depth to crater semi-minor axis length was large enough. To obtain this information, the DEM had to be queried for depth information at the crater locations to obtain crater rim height and crater depth. Craters that did not have deep basins were low in contrast and would not be detectable by a CDA.

9.2.1 Introducing noise to the crater detections

CDAs are not noise-free, often estimating crater rim locations that could be pixels off the true locations. To simulate this, we added realistic noise to our simulated CDA projected crater ellipse results, making shifts to the projected crater centre, semi-major and semi-minor axes lengths, and ellipse angle of orientation. This noise was implemented as a function of the projected semi-minor axis length, as we would expect smaller noise in smaller craters, and larger noise in larger craters. We introduce the noise through random uniform sampling, having mu set to 0 and sigma being the smaller of the two values - 2 pixels, or 20% of the semi-minor axis. Comparatively, Christian *et al.* introduce less noise in their projected ellipse parameters for problem instances taken at lower altitudes than 100km, correlating to smaller observed surface errors [4].

9.3. Simulating crater matches

The CMA was also simulated to control the number of incorrect crater matches introduced into problem instances. To achieve this, we defined what percentage of the detected craters in the problem instance should be incorrectly matched, letting N be the total number of matched craters and $M = N\times$ % of incorrectly matched craters. We then randomly selected M craters, or 2 craters if $M < 2$ or $N-3$ craters if $M > N - 3$, and matched these craters amongst themselves. While a real crater matching algorithm may incorrectly match craters outside of the set of detected craters, it is important to note that incorrect crater matches are less likely to be detected as outliers if the match is close to the true crater location. To cover this worst-case scenario, we chose to incorrectly match craters within the set of detected craters. To stress-test the benchmarked pose estimation methods, we incrementally increased the percentage of incorrectly matched craters, reducing the number of valid craters usable by each of the benchmarked pose estimators.

10. Position Uncertainty

The angular uncertainty of Range and Range-Rate (RARR) from a ground station could be as large as $0.001°$ [22]. Given the distance from the Earth to the Moon is $384,400$km, the position error of the spacecraft is calculated as

$$384,400 \times \tan(0.001°) = 6.7km \tag{39}$$

as seen in Figure 9 in supplementary material.

11. Observed surface error

Lunar survey missions are interested in estimating the camera's observed surface error. Let $\mathbf{s}_M$ be the closest point of intersection from the view direction of the camera $\mathbf{v}_M = \mathbf{R}_{(3)}$ (where $\mathbf{R}_{(3)}$ is the third row of $\mathbf{R}$) at $\mathbf{r}_M$, with a spherical Moon model with radius 1737.4km, centred at the origin of the selenographic reference frame. The observed surface error was measured in this work as the straight line distance between the two points of intersection $|\mathbf{s}^{\ddagger}_M - \mathbf{s}_M{}^*|$.

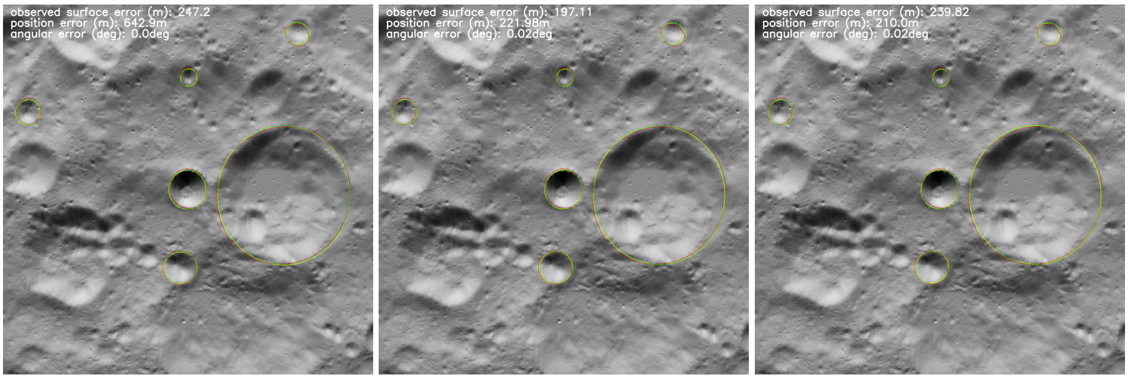

(a) 3DoF_LS (b) PnP (c) ECP

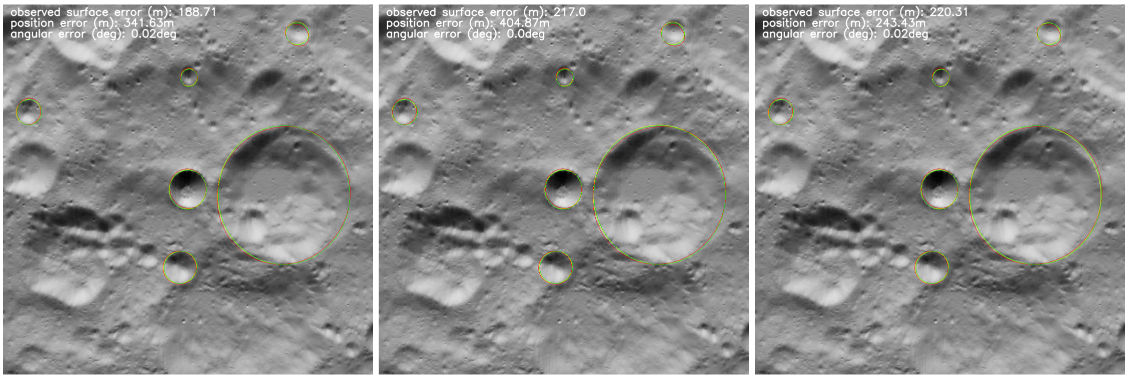

(d) EP (e) ED (f) Gauss_Ang

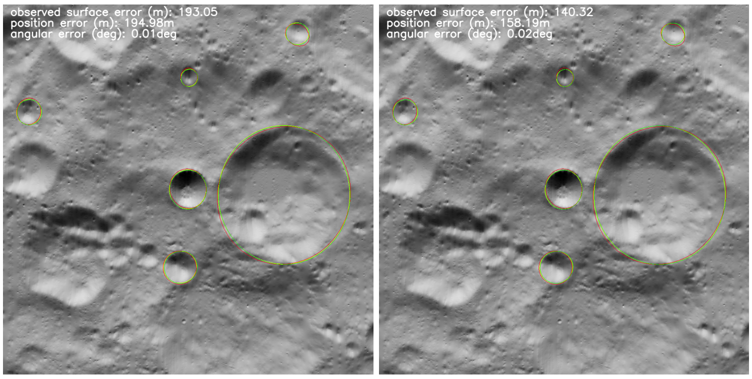

(g) L_Set (h) Wass

Figure 5. Re-projected craters under estimated pose by each benchmarked metric for a problem instance taken in the highest crater density region at an angle of 20 degrees off nadir. Green ellipses mark the ground truth crater location on the image plane, red ellipses mark the ground truth crater location with introduced noise, and yellow ellipses mark the crater locations reprojected under the estimated pose. Lunar surface images were produced using PANGU Planet Surface Simulation Software developed by the Space Technology Centre at the University of Dundee, Scotland

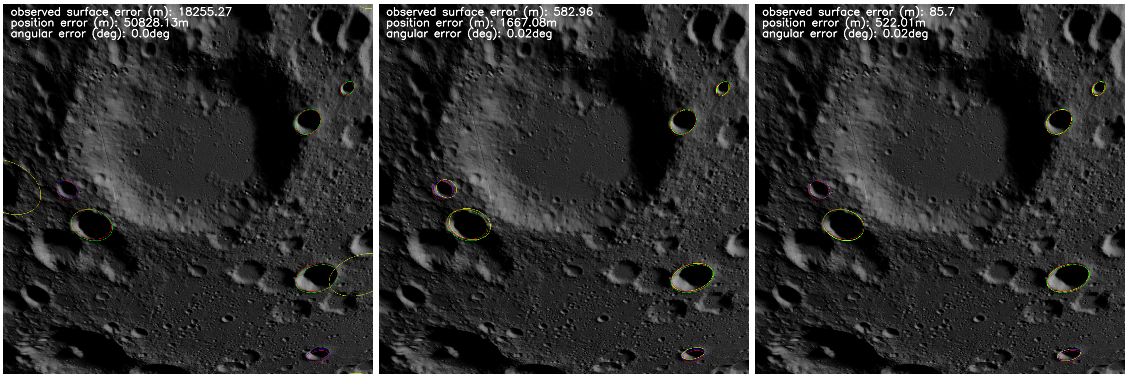

(a) 3DoF_LS (b) PnP (c) ECP

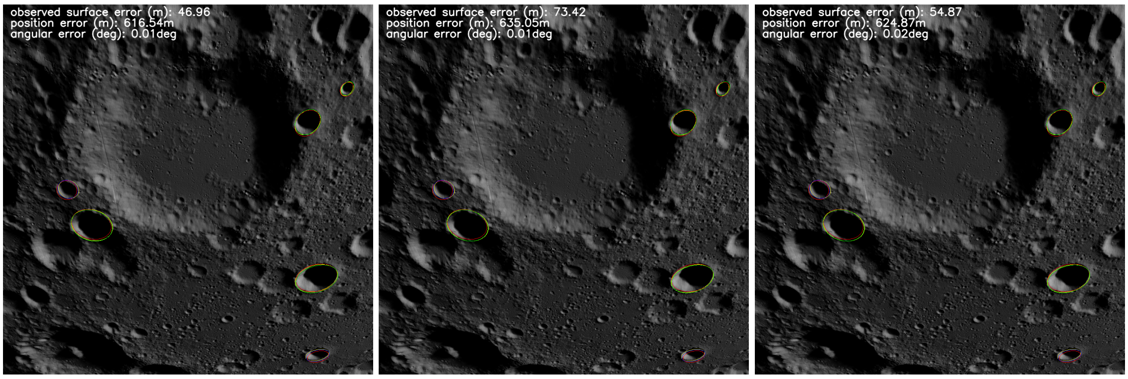

(d) EP (e) ED (f) Gauss_Ang

(g) L_Set (h) Wass

Figure 6. Re-projected craters under estimated pose by each benchmarked metric for a problem instance taken in the North Pole region at an angle of 30 degrees off nadir. Green ellipses mark the ground truth crater location on the image plane, red ellipses mark the ground truth crater location with introduced noise, blue ellipses mark incorrectly matched craters, and yellow ellipses mark the crater locations reprojected under the estimated pose. Lunar surface images were produced using PANGU Planet Surface Simulation Software developed by the Space Technology Centre at the University of Dundee, Scotland

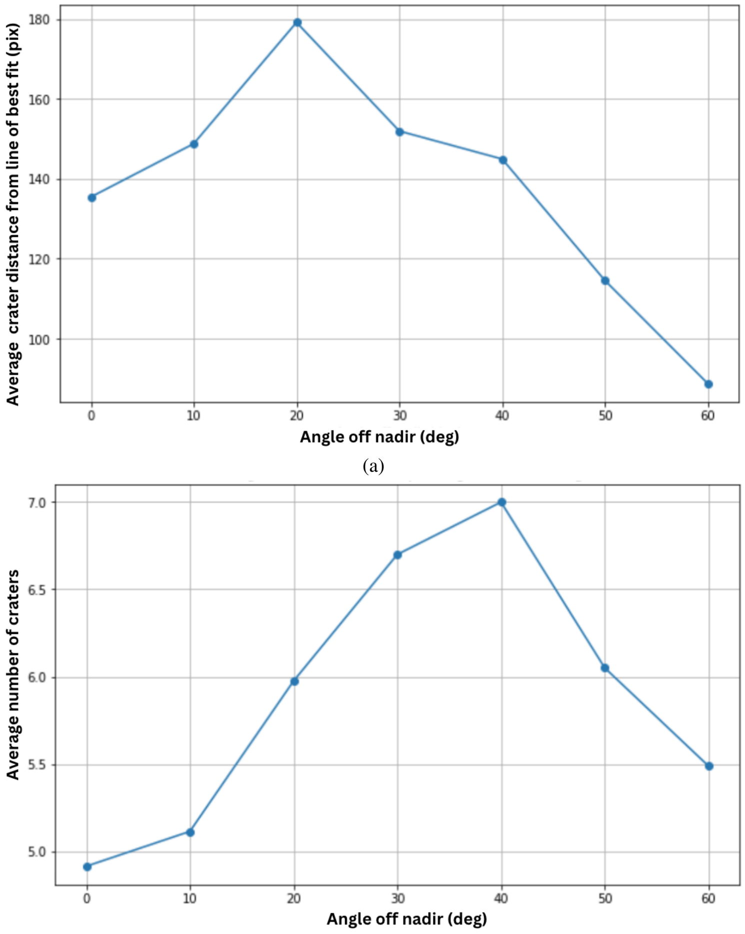

(a)

(b)

Figure 7. (a) Distribution of craters vs angle off nadir. (b) Average number of craters per problem instance vs angle off nadir.

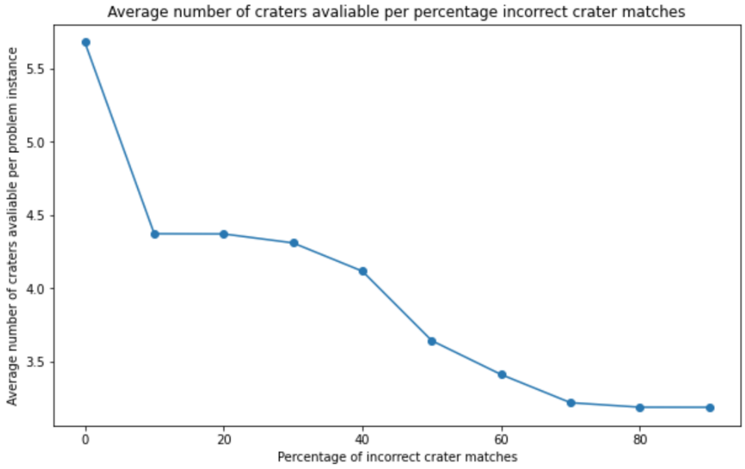

Figure 8. Average number of correctly matched craters per problem instance vs percentage of incorrectly matched craters

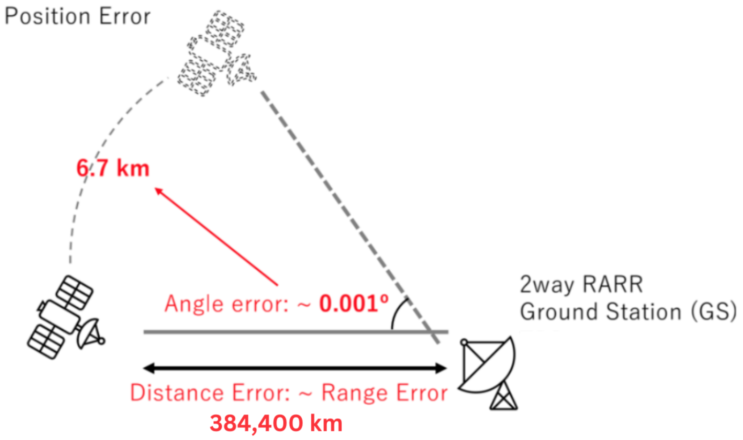

Figure 9. Diagram of how the position error is obtained.